Separation and Purification Technology 392 (2026) 137184

Contents lists available at ScienceDirect

Separation and Purification Technology

journal homepage: www.elsevier.com/locate/seppur

Ion exchange mechanism of Na-modified attapulgite for the recovery of trace Rb(I)

Na Guo [a], Huanhuan Song [a], Weiquan Zhan [a,c,**], Tianxing Chen [b], Jianbo Li [a,*], Shaoxian Song [a], Michael Badawi [c]

[a] Key laboratory of Green Utilization of Critical Non-metallic Mineral Resources of Ministry of Education, Wuhan University of Technology, Wuhan, Hubei 430070, China
[b] School of Resources Engineering, Xi'an University of Architecture and Technology, Xi'an, Shaanxi 710000, China
[c] Université de Lorraine, CNRS, Laboratoire Lorrain de Chimie Moléculaire, F-54000 Nancy, France

ARTICLE INFO

Editor: Philiswa Nomngongo

Keywords:
Rubidium
Clay
Ion exchange
Trace-level
Sustainable recovery

ABSTRACT

Rubidium (Rb) is a strategic alkali metal with increasing industrial demand and limited natural availability, making its efficient recovery from dilute aqueous systems increasingly important. In this study, Na-modified attapulgite (Na-APT), a low-cost and naturally abundant clay-based adsorbent, was developed for the rapid capture of trace Rb(I). While Na modification preserves the intrinsic crystal structure of APT, it introduces abundant exchangeable Na^+ sites that significantly accelerate mass transfer. Remarkably, Na-APT exhibits ultrafast kinetics, reaching equilibrium within seconds, and achieves nearly quantitative Rb(I) recovery at trace-level concentrations under near-neutral conditions. Kinetic analyses indicate that the process is governed by external film diffusion, with Na^+ modification effectively minimizing interfacial mass-transfer resistance. Despite a modest Langmuir adsorption capacity, Na-APT demonstrates exceptional efficiency for trace Rb(I) recovery even in complex matrices, achieving nearly complete removal from real salt-lake brine. Combined with excellent regeneration stability and low material cost, Na-APT offers a pragmatic and sustainable solution for large-scale Rb recovery from natural waters where rapid kinetics and cost-effectiveness are prioritized over high adsorption capacity.

1. Introduction

Rubidium (Rb) is a strategic and relatively rare alkali metal that has attracted growing attention due to its unique physicochemical properties and expanding range of industrial applications [1]. As one of the most electropositive elements, Rb possesses high chemical reactivity and low ionization energy, which confer excellent performance under extreme conditions, as well as good environmental compatibility [2,3]. These characteristics make Rb indispensable in a variety of high-technology fields, including atomic clocks, magnetic fluid generators, and ion propulsion systems [4]. Despite its technological importance, Rb rarely occurs as an independent mineral in nature because of its strong chemical activity [5]. Instead, it is typically present as a trace or minor component in minerals such as lepidolite and pollucite, as well as in liquid resources including salt lake brines, geothermal water, and industrial effluents [6].

However, the efficient extraction of Rb(I) remains highly challenging. Indeed, its typically low concentration, combined with the coexistence of chemically similar alkali and alkaline-earth ions, severely complicates selective separation. Conventional techniques such as precipitation [7–9], solvent extraction [10,11], and adsorption [12] have been explored for Rb recovery. However, precipitation often generates fine and poorly settleable solids, while solvent extraction suffers from process complexity, high reagent consumption, and limited selectivity. In contrast, adsorption has emerged as a particularly attractive approach for Rb(I) recovery owing to its operational simplicity, cost-effectiveness, and environmental compatibility [13]. Among various adsorbents, natural clay minerals have attracted increasing attention due to their abundance, low cost, and intrinsic ion-exchange capability [14].

Attapulgite (APT), a hydrated magnesium aluminum silicate with a unique fibrous chain-layer structure, provides abundant exchangeable sites and structural channels favorable for alkali metal uptake [15].

* Corresponding author.
** Corresponding author at: Université de Lorraine, CNRS, Laboratoire Lorrain de Chimie Moléculaire, F-54000 Nancy, France.
E-mail addresses: zhan_weiquan@163.com (W. Zhan), lijianbo3051@163.com (J. Li).

https://doi.org/10.1016/j.seppur.2026.137184
Received 28 October 2025; Received in revised form 18 January 2026; Accepted 5 February 2026
Available online 7 February 2026

Sodium-modified attapulgite (Na-APT) further amplifies these intrinsic advantages. Through ion-exchange with sodium ions, the cation-exchange capacity and surface charge density of attapulgite can be significantly improved, facilitating the adsorption of target ions from aqueous solutions [16]. Previous studies have successfully applied Na-APT and related attapulgite-based materials for the adsorption of ions such as Eu(III), Cd(II), Cr(VI), highlighting its versatility and effectiveness as an inorganic adsorbent [17–21]. Owing to the comparable ionic radius, hydration characteristics, and charge density of Rb(I), Na-APT is expected to provide favorable adsorption sites through ion-exchange and electrostatic interactions.

In this study, Na-based attapulgite was synthesized and applied as an inorganic adsorbent for Rb(I) recovery from dilute aqueous media. To the best of our knowledge, this study represents the first systematic investigation of Na-APT for Rb(I) recovery. By exploring its adsorption behavior, ion selectivity, and structural stability, this work provides new insights into the efficient utilization of natural clay minerals for strategic metal recovery. The findings are expected to contribute to the development of cost-effective, sustainable, and scalable technologies for Rb(I) extraction from complex liquid resources.

2. Experimental section

2.1. Materials

All reagents used in the study were of analytical grade. Hydrochloric acid (HCl), ammonium chloride (NH_4Cl), potassium chloride (KCl), magnesium chloride ($MgCl_2$), calcium chloride ($CaCl_2$), and sodium hydroxide (NaOH) were purchased from Sinopharm Chemical Reagents Co., Ltd. (China) and used to adjust the pH values during the preparation and adsorption processes. Rubidium chloride (RbCl) was obtained from Sigma-Aldrich and employed as the source of Rb(I) in the adsorption experiments. Deionized water with electrical resistivity of 18.2 MΩ cm was used throughout all experiments for solution preparation and washing procedures.

2.2. Materials synthesis

2.2.1. Purification of APT

Raw attapulgite was purified using a mild acid treatment to remove impurities and enhance dispersion. The raw APT sample was mixed with 4 wt% dilute hydrochloric acid at a solid-to-liquid ratio of 1:5 (g:mL). The suspension was magnetically stirred for 30 min at 25 °C, followed by ultrasonic dispersion for 1 h to promote complete disaggregation of the clay particles. Afterward, the mixture was allowed to stand for 2 h, and the upper milky suspension was carefully decanted. The collected suspension was centrifuged at 3300 rpm for 15 min to remove excess water. The obtained solid was dried at 105 °C in an oven, ground to pass through a 100−mesh sieve, and stored in a desiccator prior to modification and characterization.

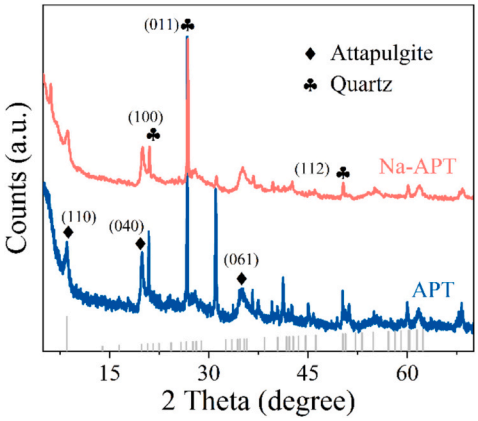

Fig. 1. XRD patterns of APT and Na-APT.

2.2.2. Preparation of Na-APT

The sodium modification of purified APT was conducted via ion exchange using NaCl solution. A 0.5 mol/L NaCl solution was first prepared, and purified APT was dispersed in this solution to obtain a suspension with a solid concentration of 40 g/L. The pH of the suspension was adjusted to 4.0, and the mixture was shaken at 30 °C with a rotation speed of 150 rpm for 24 h to ensure sufficient ion exchange. The product was then separated by centrifugation at 10000 rpm, dried at 105 °C, seized through a 100-mesh sieve, and stored in a desiccator for further use.

2.3. Adsorption experiments

Batch adsorption experiments were carried out to evaluate the Rb(I) uptake performance of APT-based adsorbents. 200 mL of an Rb(I) aqueous solution with a predetermined initial concentration was transferred into a 250 mL beaker. A prescribed amount of APT or Na-APT adsorbent was then added, and the suspension was magnetically stirred at a controlled speed for a specified contact time to ensure adsorption equilibrium.

The effects of various experimental parameters, including the initial Rb(I) concentration, adsorbent dosage, solution pH, temperature, and stirring speed, were systematically investigated to optimize the adsorption conditions. After the reaction, the suspension was separated by centrifugation, and the supernatant was collected for Rb(I) concentration analysis using atomic absorption spectrophotometer (AAS). All experiments were performed in triplicate, and the average values were used for data analysis.

Rb(I) adsorption capacity (Q) and recovery (R) for evaluating recovery performances were respectively calculated via the following equations:

$$Q = \frac{C_0 V_0 - C_t V_t}{m} \tag{1}$$

$$R = \frac{C_0 - C_t}{C_0} \times 100\% \tag{2}$$

where C_0 and C_t represent the Rb concentrations at the beginning and at time t of the adsorption process (mg/L), V_0 and V_t donate the corresponding solution volumes (L), and m is the mass of the adsorbent used in the experiment (mg).

2.4. Desorption experiments

To evaluate the recyclability of Na-APT, the desorption of Rb(I) was conducted using an NH_4Cl solution as the eluent. Specifically, the Rb-loaded Na-APT was immersed in 200 mL of 1.0 mol/L NH_4Cl solution and stirred under constant conditions. At predetermined time intervals, 1.5 mL of the solution was sampled to determine the Rb concentration using AAS. The desorption efficiency (D, %) was calculated according to the following equation:

$$D = \frac{C_d \times V_d}{C_{ad} \times V_0} \times 100\% \tag{3}$$

where C_d is the concentration of Rb(I) in the desorption solution (mg/L), V_d is the volume of the desorption solution (L), C_{ad} is the amount of Rb(I) adsorbed during the adsorption process (mg/L), and V_0 is the initial volume of the adsorption solution (L).

2.5. Materials characterizations

The crystal structure of the samples was analyzed using X-ray diffraction (XRD, D8 Advance, Bruker, AXS, Germany) with Cu Kα

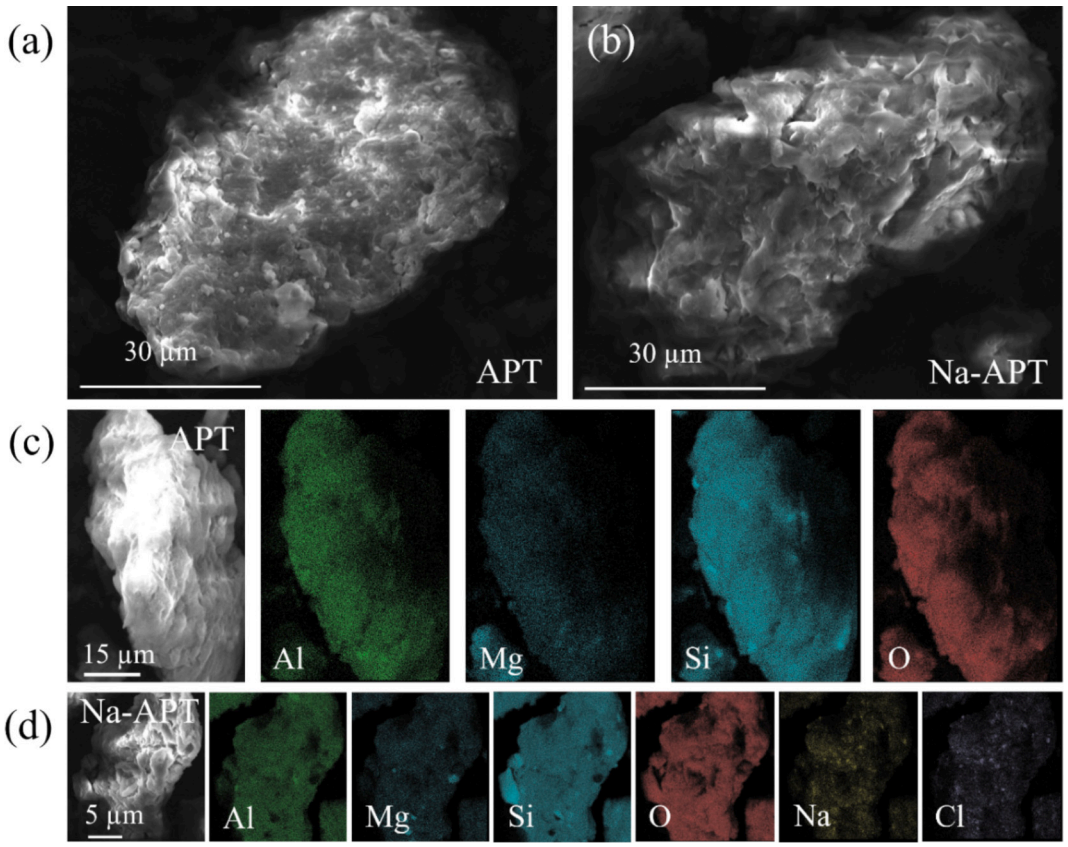

Fig. 2. SEM images (a, b) and corresponding EDS mappings (c, d) of APT and Na-APT.

radiation. Fourier transform infrared spectroscopy (FTIR) was applied to investigate the functional groups from 4000 to 400 cm^{-1} (Thermo Nicolet, USA). The surface morphology was examined by scanning electron microscopy (SEM, Phenom ProX G6, Netherlands). The chemical states and surface compositions were determined by X-ray photoelectron spectroscopy (XPS, K-Alpha, Thermo Scientific, USA). The concentration of Rb was quantified using an atomic absorption spectrometer (AAS, Agilent 280FS AA, G8434A, USA).

3. Results and discussion

3.1. Material characterization

XRD analysis was performed on both pristine APT and Na-APT to investigate their crystal structures and phase compositions. As shown in Fig. 1, the diffraction patterns of APT and Na-APT display characteristic reflections at 8.8°, 19.9°, and 35.1°, which can be indexed to the (110), (040), and (061) planes of palygorskite-type attapulgite. Furthermore, unique peaks at 21.1°, 26.8° and 50.3° were identified as the crystal planes 100, 011, 112 of SiO_2 (JCPD No. 99–0088), indicating the presence of silica impurities in the clay sample [22]. The observed peak shift between APT and Na-APT reveals an expansion of the lattice spacing after sodium treatment. This expansion is consistent with insertion/ion-exchange of Na^+ into the interlayer or channel regions of the palgorskite structure, which increases the average interplanar distance and produces the lower-angle shift in the diffraction peaks.

SEM combined with EDS was employed to analyze the surface morphology and elemental composition of APT and Na-APT (Fig. 2). Both samples exhibit the typical layer-chain structure characteristic of attapulgite, consistent with its fibrous morphology. Compared with pristine APT (Fig. 2a), Na-APT (Fig. 2b) shows a rougher and more irregular surface texture, which may be attributed to the partial exchange of cations. The EDS elemental mapping results (Fig. 2c-d) reveal that APT primarily consists of Al, Mg, Si, and O, uniformly distributed throughout the structure, while no detectable Na signal is observed, confirming the absence of Na in the raw material. After Na modification, an evident Na signal appears on the surface, confirming the successful ion-exchange process. A trace amount of Cl is also detected, likely originating from the residual NaCl used during modification.

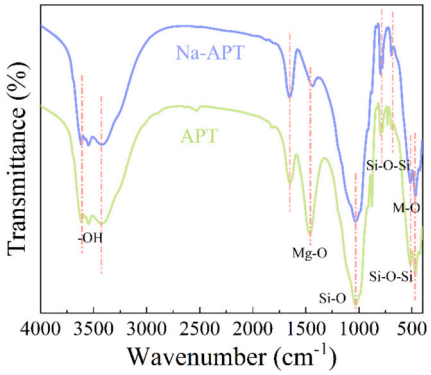

Fig. 3. FITR spectra of APT and Na-APT.

The FTIR spectra (Fig. 3) of APT and Na-APT display several characteristic absorption bands corresponding to the functional groups present in the structure. The broad bands at 3552 and 3472 cm^{-1} are associated with the stretching vibrations of −OH groups from adsorbed and structural water molecules [23]. The weak signal near 2510 cm^{-1} may originate from hydrogen-bonded −OH groups, suggesting the presence of surface hydroxyl interactions. The band observed at 1656 cm^{-1} corresponds to the bending vibration of molecular water. The peak

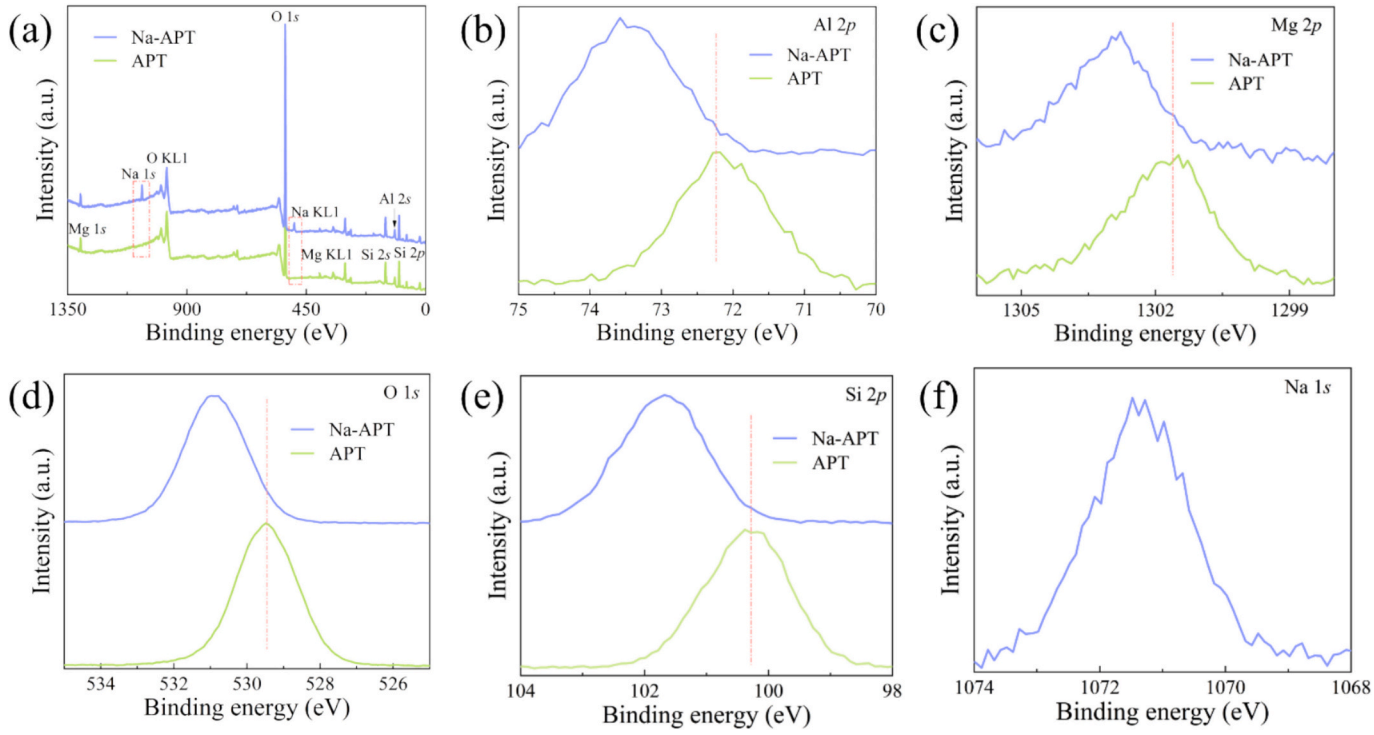

Fig. 4. Survey spectra (a) and deconvoluted high-resolution XPS spectra of Al 2*p* (b), Mg 2*p* (c), O 1 *s* (d), and Si 2*p* (e) of APT and Na-APT. High-resolution XPS spectrum of Na 1 *s* (f) of Na-APT.

at 1448 cm^{-1} can be attributed to the bending vibration of Mg—O groups within the octahedral sheet [24]. A strong absorption band at

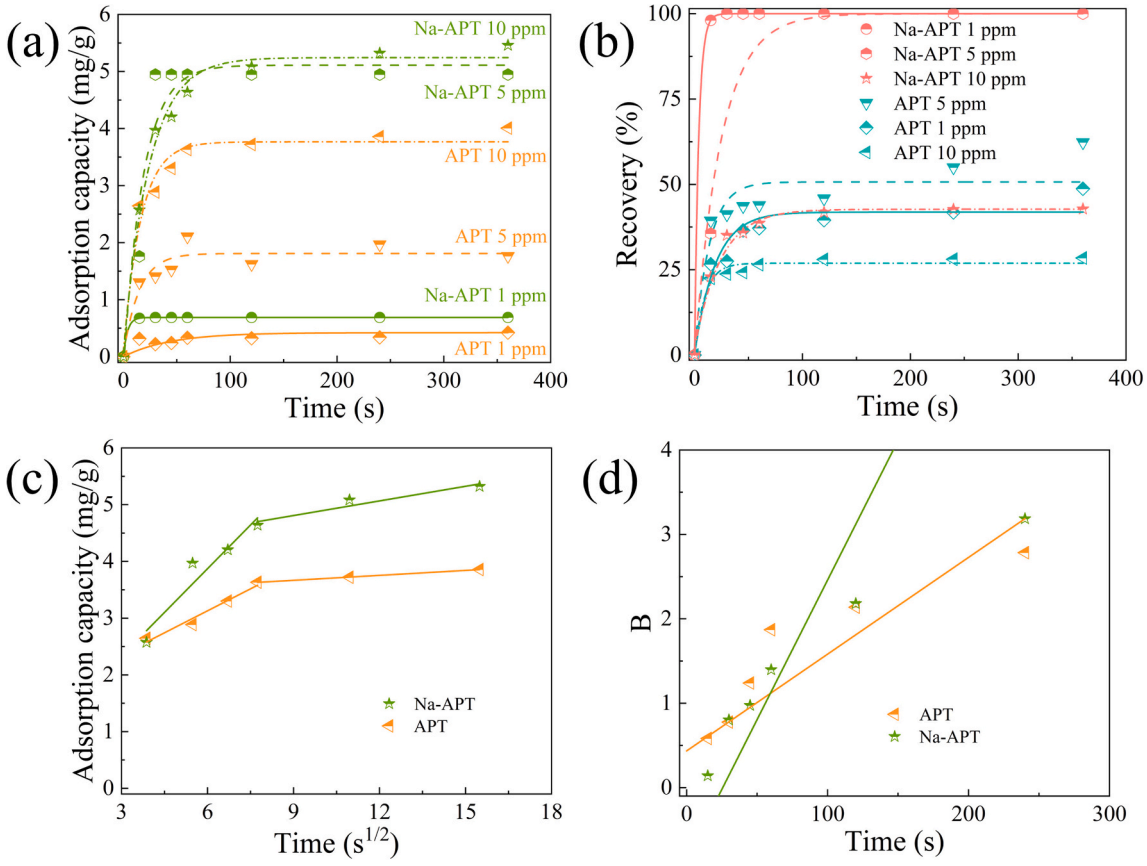

Fig. 5. Adsorption kinetics of Rb(I) on APT and Na-APT at different initial concentrations: adsorption capacity (a) and recovery (b) as a function of contact time. Fitting of the adsorption kinetics of Rb(I) on Na-APT to the (c) Weber-Morris and (d) Boyd models.

Table 1
Parameters of kinetics models of Rb(I) adsorption on APT and Na-APT.

Samples	Concentration (ppm)	Pseudo-first-order kinetic model			Pseudo-second-order kinetic model		
		k_1 (s^{-1})	q_{e1} (mg/g)	R_1^2	k_2 (g/(mg·s))	q_{e2} (mg/g)	R_2^2
APT	1	0.296	0.315	0.763	0.367	0.360	0.822
	5	0.069	1.809	0.912	0.071	1.911	0.915
	10	0.063	3.761	0.971	0.027	4.036	0.993
Na-APT	1	0.264	0.689	1	5.145	0.691	1
	5	0.052	5.112	0.923	0.015	5.527	0.870
	10	0.042	5.239	0.990	0.011	5.742	0.995

1043 cm^{-1} is assigned to the Si—O stretching vibrations in SiO_4 tetrahedra [25]. The peaks located at 801, 732, and 695 cm^{-1} are due to the symmetric stretching modes of Si−–O–Si linkages. The bands around 522 and 464 cm^{-1} are associated with the deformation and bending vibrations of Si–O–Si and M–O (M = Mg, Al, Fe) bonds, respectively, indicating that the framework structure of attapulgite remains well preserved after modification [26].

XPS analysis was conducted to investigate the surface composition and chemical states of APT and Na-APT (Fig. 4). The survey spectra (Fig. 4a) reveal both samples contain Si, Mg, Al, and O elements, while a distinct Na 1 *s* peak at 1071.36 eV appears only in the Na-APT spectrum, confirming the successful incorporation of Na^+ into the attapulgite structure through ion exchange, further being proved in Na 1 *s* spectrum (Fig. 4f). The high-resolution spectra of Al 2*p*, Mg 2*p*, O 1 *s*, and Si 2*p* (Fig. 4b-e) provide further insight into the chemical environment of these elements. For APT, the Al 2*p* and Mg 2*p* peaks are located at 72.16 and 1301.74 eV, respectively. After Na modification, these peaks shift to 73.46 and 1302.89 eV, suggesting that the introduction of Na^+ leads to a redistribution of surface charge and an increase in the binding energy of surrounding atoms. This shift can be attributed to electrostatic interactions and possible expansion of the interlayer spacing caused by Na^+ exchange. The Si 2*p* peak of APT appears at 100.06 eV, typical of Si-O-Si bonding in the silicate lattice [27], while the O 1 *s* signal centered around 529.47 eV corresponds to lattice oxygen [26,28]. In Na-APT, the Si 2*p* and O 1 *s* peaks shift to higher binding energies (101.69 and 530.88 eV), indicating stronger Si—O bond polarization and enhanced surface activity after Na modification. Collectively, these results demonstrate that Na^+ was successfully introduced into APT structure, leading to subtle electronic structure changes and potentially improving the surface activity of Na-APT.

3.2. Adsorption kinetics of Rb(I)

The kinetic behavior of Rb(I) uptake on both APT and Na-APT was investigated (Fig. 5a and b). All kinetic experiments were performed in triplicate, and the results are presented as the mean values. A common feature observed is the instantaneous adsorption stage, with nearly quantitative recovery achieved within 30 s across all tested concentrations. This ultrafast performance indicates that the adsorption process is primarily governed by highly accessible active sites and rapid ion-exchange dynamics. However, it is important to note that when equilibrium is reached so rapidly, the kinetic parameters derived from pseudo-first-order and pseudo-second-order kinetic models (Table 1) may be instrumentally limited. The variations in R^2 and the slight inconsistencies in model superiority are likely artifacts of the limited number of data points available during the transient phase (0–30 s). Rather than strictly defining a reaction order, these kinetic results collectively demonstrate that Na-modification preserves and enhances the fast mass-transfer pathways of the APT framework. The high magnitude of the rate constants for both adsorbents underscores their suitability for high-throughput or continuous-flow water treatment, where short contact times are essential.

An additional systematic trend is that the apparent adsorption rate constants decrease with increasing initial Rb(I) concentrations. This concentration-dependent kinetic behavior is primarily attributed to progressive site saturation and enhanced mass-transfer resistance. At higher solute loadings, a finite number of readily accessible exchange sites must accommodate a larger population of Rb(I) ions, which reduces the effective uptake rate and slows the approach to equilibrium. Although the equilibrium adsorption capacities increase with increasing initial concentration, the recovery tends to decrease because a fixed number of exchange sites can remove only a diminishing fraction of the total Rb(I) present in solution. This explains why both APT and Na-APT show higher percentage recovery at low concentrations, in fact, Na-APT achieves essentially complete recovery at 1 and 5 ppm, whereas recovery declines at 10 ppm. Taken together, Na-APT is highly effective for trace-level Rb(I) adsorption, with extremely fast uptake kinetics that are advantageous for practical treatment of dilute streams.

Table 2
Intraparticle diffusion parameters in first step from the Weber-Morris model for Rb(I) adsorption on APT and Na-APT.

Samples	K_{id} (mg g^{-1} $s^{0.5}$)	R^2
APT	0.258	0.984
Na-APT	0.513	0.958

Table 3
Boyd model parameters for Rb(I) adsorption on APT and Na-APT.

Samples	Slope (s^{-1})	Intercept	R^2
APT	0.011	0.435	0.889
Na-APT	0.033	−0.847	0.913

To gain deeper mechanistic insight into the rate-controlling steps, the intraparticle diffusion model (Weber-Morris) and Boyd model were further employed. The intraparticle diffusion plots (Fig. 5c) exhibit multilinear behavior for both APT and Na-APT, indicating that Rb(I) uptake proceeds via multiple sequential steps rather than a single

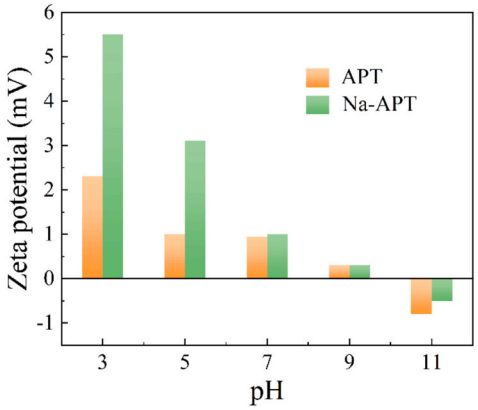

Fig. 6. Zeta potential of APT and Na-APT at various pH values.

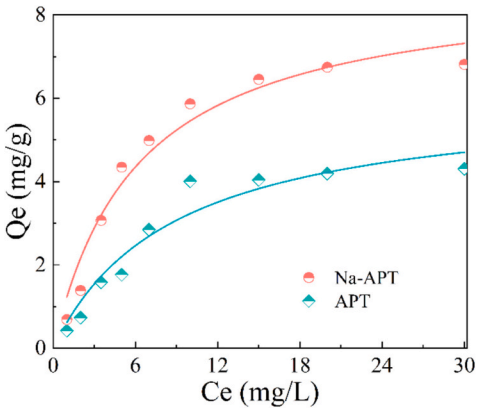

Fig. 7. Adsorption isotherm of Rb(I) on APT and Na-APT.

diffusion-controlled process. Notably, the intraparticle diffusion rate of Na-APT is approximately twice that of APT (Table 2), suggesting a substantially enhanced internal mass-transfer rate after Na^+ modification. The non-zero intercepts further indicate that boundary-layer diffusion contributes significantly to the overall adsorption kinetics. Boyd analysis provides additional clarification of the rate-limited step. As shown in Fig. 5d and Table 3, both APT and Na-APT do not pass through the origin, confirming that external film diffusion rather than intraparticle diffusion dominates the overall adsorption rate under the investigated conditions.

These kinetic differences can be rationalized by Na^+ induced structural and interfacial modifications. As evidenced by the XRD peak shifts toward lower diffraction angle, Na^+ modification leads to lattice relaxation associated with Na^+ exchange within the structural channels and enhanced channel hydration. These structural changes enlarge the effective diffusion pathways within the channels and reduce the steric and hydration-related resistance for incoming Rb(I) ions. In addition, zeta potential measurements (Fig. 6) reveal that Na-APT exhibits a higher surface potential than APT, reflecting the successful preloading of exchangeable Na^+ on the surface. This modification indicates a reconstructed interfacial charge environment that facilitates rapid Na^+-Rb(I) ion exchange and reduces the interfacial mass-transfer resistance. Collectively, these structural and interfacial changes accelerate ion mobility and exchange dynamics, leading to faster uptake kinetics for Na-APT.

The equilibrium adsorption behavior of Rb(I) on both APT and Na-APT was further evaluated using the Langmuir, Freundlich, and Temkin isotherm models (Eq. 4–6, Fig. 7, and Table 4). Overall, the adsorption of Rb(I) on both materials is well represented by the Langmuir model, as indicated by the highest correlation coefficients,

Table 4
Fitting results from Langmuir, Freundlich, and Temkin models for Rb(I) adsorption on APT and Na-APT.

Samples	Langmuir			Freundlich			Temkin		
	Qm (mg/g)	KL (L/mg)	R^2	n	KF (mg/g)	R^2	B (J/Mol)	KT (L/g)	R^2
APT	6.088	0.113	0.937	2.061	0.963	0.865	1.357	1.080	0.929
Na-APT	8.820	0.162	0.962	2.373	1.881	0.921	2.038	1.378	0.959

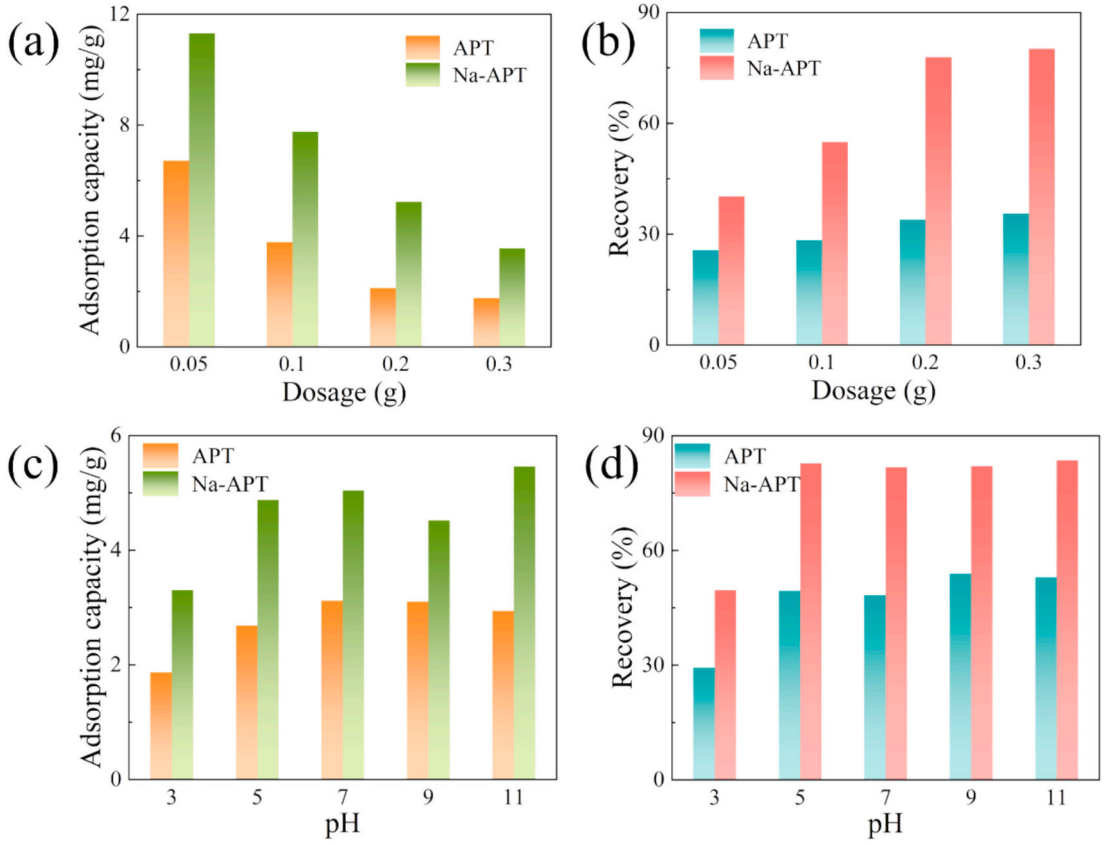

Fig. 8. Effect of adsorbent dosage on adsorption capacity (a) and recovery (b) of Rb(I). Effect of solution pH on adsorption capacity (c) and recovery (d) of Rb(I).

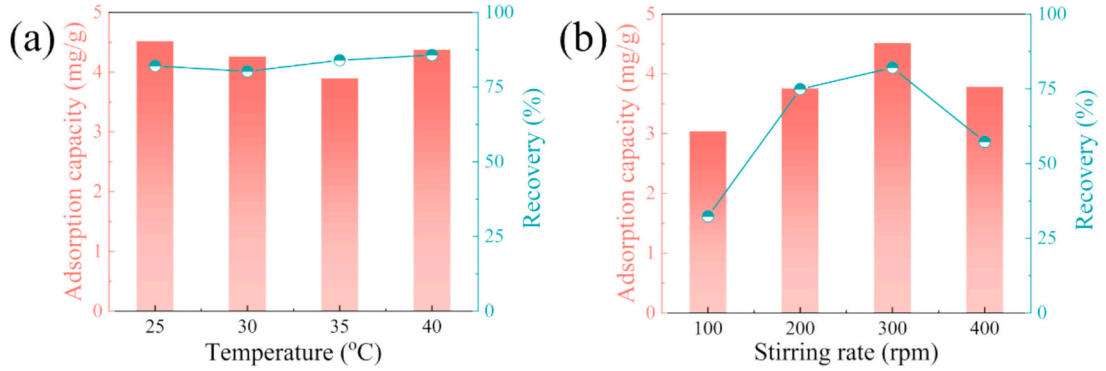

Fig. 9. Effect of reaction temperature (a) and stirring rate (b) on the adsorption performance of Na-APT toward Rb(I).

suggesting that Rb(I) uptake predominantly proceeds through monolayer adsorption onto a finite number of energetically homogeneous sites. Consistent with this interpretation, the Langmuir-derived maximum adsorption capacities reveal that Na-APT has a slightly higher affinity toward Rb(I) than APT, in line with the enhanced ion-exchange propensity introduced by Na^+ preloading.

The Freundlich model also provides reasonable fits for both materials, though with lower R^2 value, indicating the presence of mild surface heterogeneity. The Freundlich exponent n exceeds unity for both APT and Na-APT, confirming that Rb(I) adsorption is favorable over the tested concentration range. Meanwhile, the Temkin model captures the influence of adsorbate-adsorbent interactions, with Na-APT exhibiting a larger Temkin constant B compared to APT, suggesting that Na-APT experiences slightly stronger adsorbate interaction energies as equilibrium is approached.

$$\frac{C_e}{q_e} = \frac{1}{(q_m \times K_L)} + \frac{C_e}{q_m} \tag{4}$$

$$\ln q_e = \ln K_F + \frac{1}{n} \times \ln C_e \tag{5}$$

$$q_e = B \times \ln K_T + B \times \ln C_e \tag{6}$$

where q_e (mg/g) is the adsorption capacity at equilibrium concentration (C_e, mg/L). q_m is the maximum adsorption capacity (mg/g) from Langmuir model. K_L (L/mg), K_F (mg/g), and K_T (L/g) are the constant in Langmuir, Freundlich, and Temkin model, respectively. n is a constant related to the adsorption intensity. B is a constant representing sorption heat (J/mol).

Na-APT possesses more accessible and energetically favorable exchange sites, leading to higher uptake capacity and faster adsorption kinetics. The dominance of Langmuir-type behavior highlights that Rb(I) adsorption is primarily governed by monolayer ion-exchange rather than multilayer accumulation.

3.3. Effect of experimental parameters

The influence of adsorbent dosage and solution pH on the Rb(I) adsorption performance of APT and Na-APT is shown in Fig. 8a-d. As seen in Fig. 8a, the adsorption capacity of both adsorbents decreases with increasing dosage. This inverse relationship arises because a higher adsorbent mass provides a greater number of total adsorption sites, but simultaneously decreases the Rb(I) concentration per unit mass and reduces the driving force for mass transfer. Consequently, at higher dosages, more sites remain unoccupied, leading to a lower specific adsorption capacity. Nevertheless, as shown in Fig. 8b, the recovery of Rb(I) increases with increasing dosage, indicating that the total number of captured Rb(I) rises even though the efficiency per gram of adsorbent declines.

The effect of pH on adsorption is illustrated in Fig. 8c-d. The adsorption capacity of both APT and Na-APT increases steadily from pH 3 to 11. At low pH values, excess H^+ compete strongly with Rb(I) for negatively charged surface sites, suppressing adsorption. As the pH increases, deprotonation of surface hydroxyl groups enhances the electrostatic attraction and ion-exchange between Rb(I) and the negatively charged silanol/aluminol sites, leading to higher adsorption. Na-APT consistently shows higher Rb(I) uptake and recovery than APT throughout the pH range, confirming that Na-exchange treatment effectively increases the number of active exchangeable sites and improves surface charge characteristics favorable for Rb(I) adsorption.

The influence of reaction temperature and stirring speed on the adsorption performance of Na-APT toward Rb(I) is presented in Fig. 9. As shown in Fig. 9a, the adsorption capacity and recovery remained nearly constant with increasing temperature from 20 °C to 45 °C, indicating that the adsorption of Rb(I) onto Na-APT is relatively insensitive to temperature within this range. This weak temperature dependence

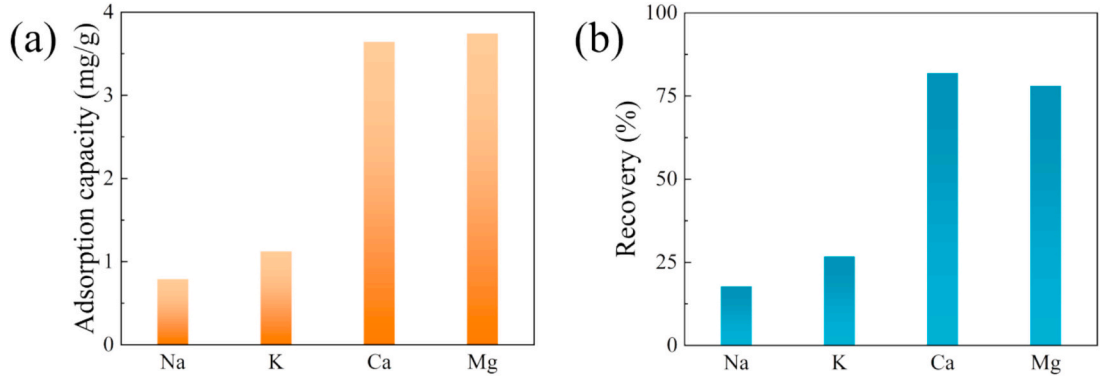

Fig. 10. Selective adsorption capacity (a) and recovery (b) of Na-APT toward Rb(I) in the presence of competing cations.

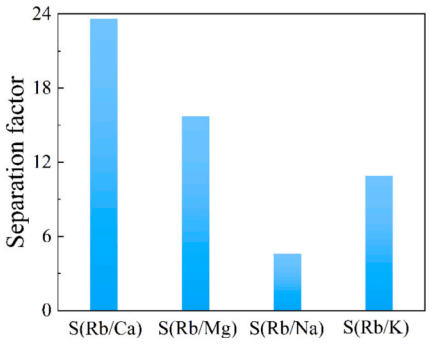

Fig. 11. Separation factors of Rb(I) in the various solutions containing cations.

Table 5
Chemical composition and properties of the real salt-lake brine.

Component	Mg	K	Na	Li	Ca	Rb
Concentration (ppm)	101,732	2292	1930	94	68	0.16

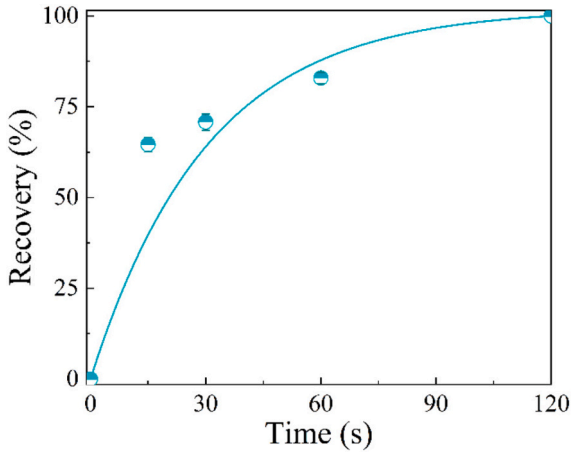

Fig. 12. Recovery performance of Na-APT for trace Rb(I) from real salt lake brine.

suggests that the adsorption process is mainly dominated by physical adsorption or ion exchange rather than a strongly endothermic chemisorption mechanism. As shown in Fig. 9b, the stirring rate exhibited a more pronounced effect. The adsorption capacity and recovery increased significantly as the stirring rate rose from 100 to 300 rpm, which can be attributed to enhanced mass transfer and better contact between Rb(I) and the active sites on Na-APT. However, when the stirring rate further increased to 400 rpm, both adsorption capacity and recovery slightly decreased, likely due to the disturbance or desorption of weakly bound Rb(I) caused by excessive agitation. Therefore, a moderate stirring rate was found to be optimal for achieving efficient and stable Rb(I) adsorption.

3.4. Selective adsorption behavior and practical Rb(I) recovery

To evaluate the applicability of Na-APT for Rb(I) recovery under realistic conditions, selective adsorption experiments were conducted in the presence of common coexisting cations, including Na^+, K^+, Ca^{2+}, and Mg^{2+}. As shown in Fig. 10, the presence of competing ions significantly affects the Rb(I) recovery performance of Na-APT. To further quantify the affinity of Na-APT, separation factors were calculated (Fig. 11). In the presence of Ca^{2+} or Mg^{2+}, Na-APT maintains high separation factors significantly higher than those for monovalent ions. These results indicate that divalent metal ions exert a much weaker inhibitory effect on Rb(I) uptake, likely due to their hydrated radii and different exchange site preference. In contrast, the Rb(I) recovery decreases when Na^+ or K^+ is present. This pronounced suppression is primarily attributed to the strong competition between alkali metal ions for the same exchangeable sites on Na-APT. Particularly in the Na^+ system, the high background concentration and the effect of preloaded Na^+ significantly shift the ion-exchange equilibrium, thereby limiting the extent of Rb(I) uptake. Nevertheless, the fact that all competing ions confirm the inherent preferential affinity of Na-APT for Rb(I), a property that is further validated by the nearly quantitative recovery achieved in complex real brine matrices.

To evaluate the practical applicability of Na-APT, adsorption experiments were performed using actual salt lake brine (Table 5) with a trace Rb(I) concentration of 0.16 ppm. The experiments were conducted at a dosage of 0.3 g Na-APT and a natural pH of 6.3. To ensure data reliability, the tests were performed in triplicate Despite the extremely high salinity and high concentrations of competing ions, Na-APT achieved nearly complete Rb(I) recovery (Fig. 12). The stable performance in such a complex matrix, combined with the low adsorbent dosage required, confirms that Na-APT possesses exceptional affinity for Rb(I) and high tolerance to background electrolytes, making it a robust candidate for industrial Rb(I) extraction from natural brine resources.

Although the selective adsorption experiments reveal that coexisting metal ions can reduce the apparent adsorption capacity of Na-APT by suppressing ion-exchange efficiency, this effect does not compromise its effectiveness for trace-level Rb(I) recovery. Under dilute conditions, the number of available exchange sites on Na-APT remains sufficient to capture Rb(I) quantitatively, demonstrating the strong practical

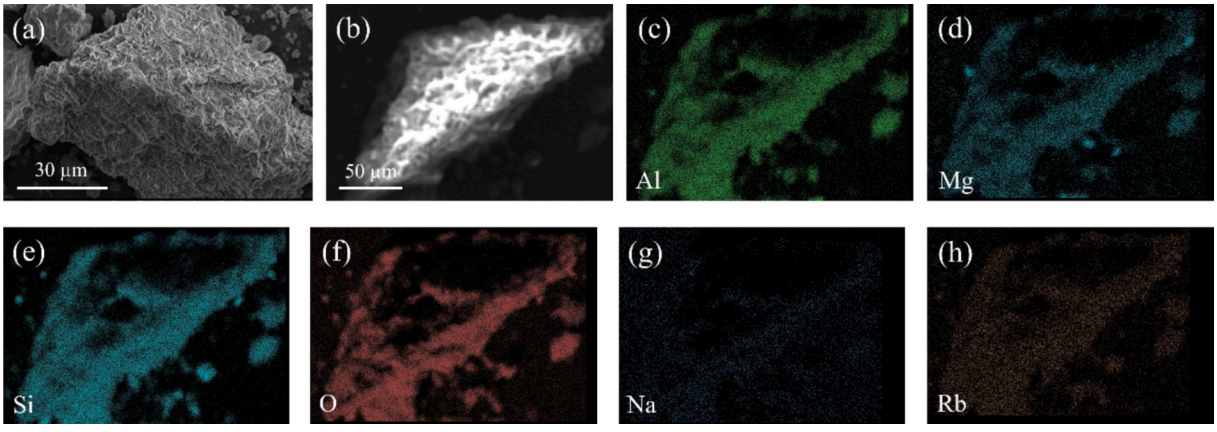

Fig. 13. SEM images (a, b) and corresponding EDS mappings (c, d) of Na-APT after Rb(I) adsorption.

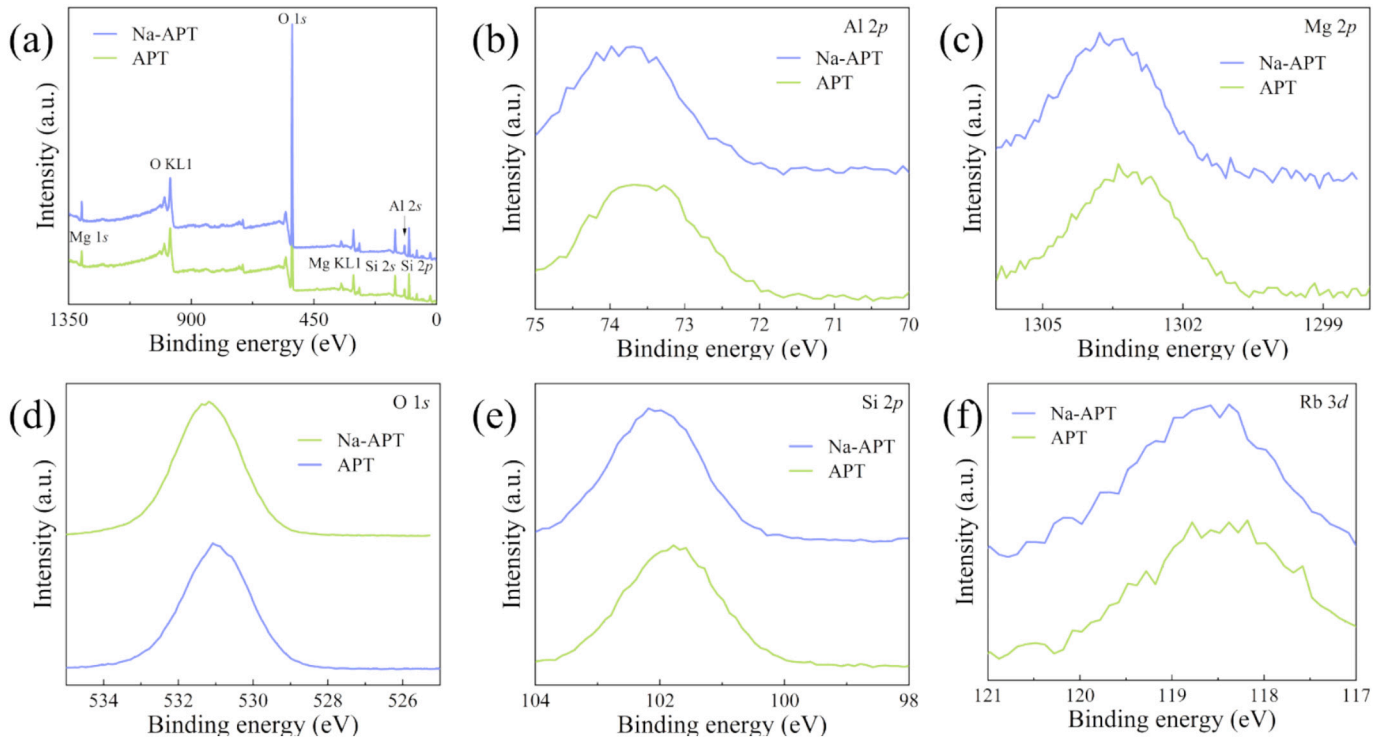

Fig. 14. Survey spectra (a) and deconvoluted high-resolution XPS spectra of Al 2*p* (b), Mg 2*p* (c), O 1 *s* (d), Si 2*p* (e), and Rb 3*d* (f) of APT and Na-APT after Rb (I) adsorption.

potential of Na-APT for real-water applications.

3.5. Characterization after adsorption

The surface morphologies of Na-APT after Rb(I) adsorption were examined by SEM, as shown in Fig. 13. The Na-APT sample retained its fibrous and porous structure after adsorption, with no significant change in morphology observed (Fig. 13a-b). This suggests that the adsorption process did not destroy or alter the original framework of the material, indicating that Rb(I) uptake mainly occurred through surface ion-exchange or electrostatic interactions rather than structural reconstruction or chemical corrosion. Furthermore, the EDS elemental mapping (Fig. 13c-g) shows that the elemental composition and distribution of Na, Mg, Al, Si, and O retained nearly uniform before and after adsorption. Importantly, the appearance of a distinct Rb signal (Fig. 13h) in the post-adsorption EDS spectrum confirms the successful adsorption of Rb(I) on the Na-APT surface. The homogeneous distribution and that the adsorption process proceeds in a surface-controlled and highly efficient manner.

The XPS spectra of APT and Na-APT after Rb(I) adsorption are shown in Fig. 14. As illustrated in the survey spectra (Fig. 14a), the main characteristic peaks corresponding to Al, Mg, Si, and O remained nearly identical to those observed before adsorption, indicating that the overall chemical composition and structure of the materials were well preserved. However, the Na signal on Na-APT became much weaker or nearly disappeared after adsorption. This phenomenon can be attributed to the ion-exchange process between Na^+ and Rb(I), in which Rb(I) from the solution replace Na^+ in the interlayer or surface exchangeable sites of Na-APT. Consequently, the enrichment of Rb(I) and the reduction of Na^+ on the surface confirm that the adsorption is primarily driven by ion exchange rather than simple physical adsorption.

In the high-resolution spectra (Fig. 14b-e), the binding energies of Al 2*p*, Mg 2*p*, O 1 *s*, and Si 2*p* in both APT and Na-APT showed a slight positive shift after Rb(I) adsorption. These shifts suggest a change in the local electronic environment, likely due to the electrostatic interaction and partial charge transfer between Rb(I) and the oxygen-containing groups or the silicate framework of attapulgite. Importantly, a distinct new peak at ~118.38 eV (Fig. 14f) was detected in both samples, which corresponds to the Rb 3d orbital of adsorbed Rb(I) [29]. The presence of this Rb peak provides direct evidence for the successful adsorption of Rb

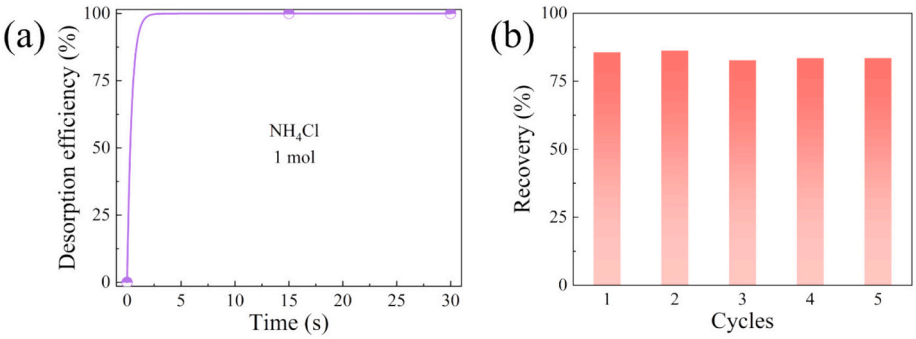

Fig. 15. The desorption efficiency of Rb(I) from Rb(I)-loaded Na-APT (a) and adsorption-desorption cycles of Rb(I) on Na-APT (b).

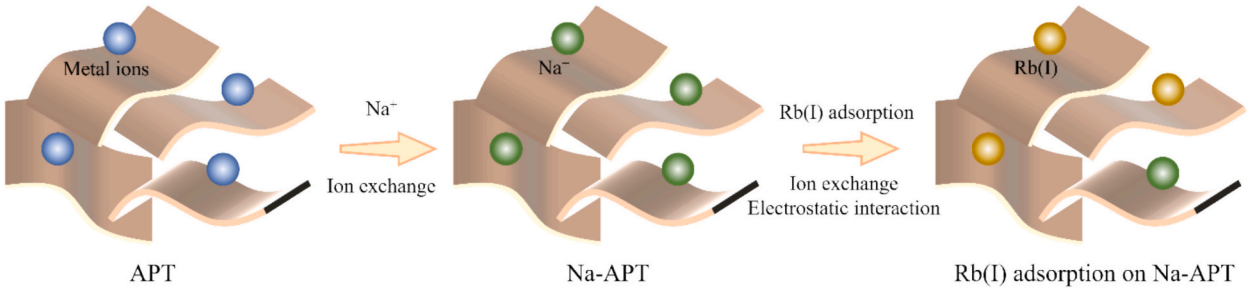

Fig. 16. Schematic illustration of the mechanism of Rb(I) adsorption on Na-APT.

(I) on APT and Na-APT surfaces. Overall, these XPS results confirm that Rb(I) adsorption occurs mainly through ion exchange and surface complexation processes, accompanied by minor electronic structure perturbations in the framework elements (Si, Al, Mg, O) without significant chemical degradation of the host materials.

3.6. Adsorption-desorption cycles

As presented in Fig. 15a, the desorption process occurred rapidly, reaching nearly 100% desorption efficiency within only 15 s. This remarkable performance demonstrates that Rb(I) can be completely and efficiently released from the Na-APT surface by simple ionic exchange with NH_4^+ ions. The strong driving force of NH_4^+ for cation exchange and the high mobility of Rb(I) in the hydrated interlayers jointly contributed to this fast desorption behavior. The results indicate that the adsorption of Rb(I) on Na-APT is a reversible ion-exchange process, rather than an irreversible chemical fixation. Moreover, the efficient regenation without the need for harsh chemical agents implies a low-cost and environmentally friendly process, which is promising for practical implementation in large-scale Rb recovery systems. In Fig. 15b, Na-APT exhibits excellent regeneration performance during repeated adsorption-desorption cycles. After five consecutive adsorption-desorption cycles, the Rb(I) recovery of Na-APT remains nearly unchanged, indicating negligible performance degradation and outstanding structural stability of the adsorbent.

3.7. Proposed mechanism of Rb(I) adsorption

The adsorption of Rb(I) onto Na-APT predominantly proceeds via an ion-exchange mechanism (Fig. 16). Na-APT contains abundant exchangeable Na^+ distributed within its structural channels and on the external surface, where they are coordinated to oxygen atoms and hydroxyl groups in the layered silicate framework. Upon contact with Rb(I) containing solution, Rb(I) with a relatively large ionic radius and low hydration energy can effectively replace the pre-existing Na^+ in these exchangeable sites. In addition, in Na-APT, the pre-intercalation of Na^+ increases the number of exchangeable sites, facilitating faster diffusion and higher Rb(I) uptake compared with pristine APT. The ion-exchange process is further substantiated by XPS analysis, which reveals a pronounced decrease in the Na signal accompanied by the emergence of distinct Rb peaks after adsorption, directly confirming the replacement of Na^+ by Rb(I). Meanwhile, minor binding energy shifts in Si, Al, and O indicate partial surface complexation and local charge redistribution upon Rb(I) binding. This process is thermodynamically favorable due to the high affinity of Rb(I) for negatively charged surface sites and its ability to form stable electrostatic interactions with oxygen atoms in the Si—O and Al—O structural units. Overall, the adsorption mechanism of Rb(I) on Na-APT can be attributed to ion exchange coupled with electrostatic attraction, leading to efficient and stable Rb(I) immobilization on the adsorbent surface.

4. Conclusions

In summary, Na-APT was successfully developed as a cost-effective and high-speed adsorbent for Rb(I) recovery. Na modification preserves the intrinsic structure of APT while substantially improving its adsorption performance by introducing abundant exchangeable Na^+ sites and reconstructing the interfacial charge environment. As a result, Na-APT exhibits exceptional performance at trace concentrations and its ultrafast response, reaching equilibrium within seconds. These characteristics are attributed to the reconstructed interfacial charge and increased exchangeable Na^+ sites, which significantly promote film diffusion and ion-exchange dynamics. Experimental results confirm that Na-APT can achieve nearly quantitative recovery from real salt lake brine, maintaining robust selectivity and stability over multiple cycles. Instead of pursuing high equilibrium capacity, this study highlights a shorter-contact-time strategy using an inexpensive mineral. The combination of low cost, rapid kinetics, and high efficiency for dilute systems positions Na-APT as a highly competitive candidate for the sustainable and scalable extraction of Rb from natural brine and secondary resources.

CRediT authorship contribution statement

Na Guo: Writing – original draft, Methodology, Investigation, Formal analysis. **Huanhuan Song:** Methodology, Investigation. **Weiquan Zhan:** Writing – review & editing, Supervision, Investigation, Conceptualization. **Tianxing Chen:** Validation. **Jianbo Li:** Writing – review & editing, Supervision. **Shaoxian Song:** Methodology, Conceptualization. **Michael Badawi:** Conceptualization, Formal analysis, Supervision, Writing – review & editing.

Declaration of competing interest

The authors declare that they have no known competing financial interests or personal relationships that could have appeared to influence the work reported in this paper.

Acknowledgement

This work was financially supported by the National Natural Science Foundation of China (No. 22578349). Michael Badawi acknowledges Wuhan University of Technology for this two-week visiting professorship in September 2025.

Data availability

Data will be made available on request.

References

[1] Y. Wang, Q. Zhang, D. Fang, K. Li, Z. Song, W. Han, J. Li, X. Ye, H. Liu, H. Zhang, X. Zhang, Z. Wu, Selective adsorption of Rb^+ and Cs^+ by a superparamagnetic

Fe_3O_4@FeMn-MOF from brine, Desalination 600 (2025) 118481, https://doi.org/10.1016/J.DESAL.2024.118481.
[2] X. Sun, Q. Shi, W. Liu, L. Su, Y. Shen, W. Lei, J. Li, X. Meng, Z. Zhang, Efficiently selective adsorption Rb(I) based on ion-imprinted membrane chromatography: batch adsorption and dynamic filtration, Sep. Purif. Technol. 354 (2025) 128707, https://doi.org/10.1016/J.SEPPUR.2024.128707.
[3] C. Chen, W. Gao, H. Fan, X. Huang, Z. Tong, Facile single-step synthesis of $ZnFe_2O_4$@biochar for synergistic adsorption and photo-Fenton degradation of RB and RBR binary dyes, J. Taiwan Inst. Chem. Eng. 163 (2024) 105641, https://doi.org/10.1016/J.JTICE.2024.105641.
[4] Y. Zhu, W. Wang, H. Zhang, X. Ye, Z. Wu, A. Wang, Fast and high-capacity adsorption of Rb^+ and Cs^+ onto recyclable magnetic porous spheres, Chem. Eng. J. 327 (2017) 982–991, https://doi.org/10.1016/J.CEJ.2017.06.169.
[5] T. Lu, Y. Zhu, Y. Qi, Y. Kang, A. Wang, Tunable superporous magnetic adsorbent prepared via eco-friendly Pickering MIPEs for high-efficiency adsorption of Rb^+ and Sr^{2+}, Chem. Eng. J. 368 (2019) 988–998, https://doi.org/10.1016/J.CEJ.2019.03.040.
[6] Y. Wang, K. Li, L. Ma, D. Fang, M. Lu, X. Ye, H. Liu, H. Zhang, X. Tan, Z. Wu, A magnetic adsorbent with metal-organic framework based on ammonium phosphomolybdenum heteropoly tungstate (AWP): selective adsorption of Rb^+ and Cs^+ from aqueous resources and stripping with ammonium salts, Hydrometallurgy 216 (2023) 106011, https://doi.org/10.1016/J.HYDROMET.2022.106011.
[7] C. Li, K. Li, S. Li, R. Ma, Co-precipitation of Rb^+ and Cs^+ by double center ion copper-zinc hexacyanoferrate from high Na^+ and K^+ solution, Chem. Phys. Lett. 876 (2025) 142226, https://doi.org/10.1016/J.CPLETT.2025.142226.
[8] A.K. Pabby, A.M. Sastre, J.L. Cortina, Cleaner processing techniques for rubidium extraction and recovery: a critical review, J. Clean. Prod. 525 (2025) 146523, https://doi.org/10.1016/J.JCLEPRO.2025.146523.
[9] Y. Fan, D. Gao, D. Li, D. Zeng, Dissolution and recrystallization of alum to separate cesium, rubidium and potassium using their different precipitation kinetics to reach higher purity than solubility equilibria based purity of $MAl(SO_4)_2$ (M = Cs, Rb, K), Hydrometallurgy 233 (2025) 106454, https://doi.org/10.1016/J.HYDROMET.2025.106454.
[10] C. Dagan-Jaldety, P. Nativ, Y.S. Cristal, O. Lahav, A Prussian-blue analogue (PBA) ion-chromatography-based technique for selective separation of Rb^+ (as RbCl) from brines, Water Res. 247 (2023) 120757, https://doi.org/10.1016/J.WATRES.2023.120757.
[11] Z. Shuiping, L. Donghui, W. Wei, C. Xiaopeng, Z. Wengze, T. Wen, Efficient extraction of Li and Rb from zinnwaldite via thermal activation and acid leaching, Miner. Eng. 216 (2024) 108898, https://doi.org/10.1016/J.MINENG.2024.108898.
[12] G. Liu, H. Mei, X. Tan, H. Zhang, H. Liu, M. Fang, X. Wang, Enhancement of Rb^+ and Cs^+ removal in 3D carbon aerogel-supported $Na_2Ti_3O_7$, J. Mol. Liq. 262 (2018) 476–483, https://doi.org/10.1016/J.MOLLIQ.2018.04.117.
[13] K. Li, J. Xie, Z. Shi, C. Min, Z. Yin, R. Ma, S. Li, Cheap and easily separate Cs(I) and Rb(I) from high salty solution by forming RbCs–MgHCF, J. Clean. Prod. 425 (2023) 139007, https://doi.org/10.1016/J.JCLEPRO.2023.139007.
[14] L. Sellaoui, E.P. Hessou, M. Badawi, M.S. Netto, G.L. Dotto, L.F.O. Silva, F. Tielens, J. Ifthikar, A. Bonilla-Petriciolet, Z. Chen, Trapping of Ag^+, Cu^{2+}, and Co^{2+} by faujasite zeolite Y: new interpretations of the adsorption mechanism via DFT and statistical modeling investigation, Chem. Eng. J. 420 (2021) 127712, https://doi.org/10.1016/J.CEJ.2020.127712.
[15] J. Cao, Y. Liu, X. Xie, X. Shi, Y. Chen, Y. Chen, L. Xu, H. Peng, Z. Zhang, Large-scale preparation of Na_2CO_3-modified attapulgite adsorbents for efficient removal of p-nitrophenol in wastewater, Sep. Purif. Technol. 359 (2025) 130802, https://doi.org/10.1016/J.SEPPUR.2024.130802.
[16] J. Yang, K. Zhang, Z. Yang, Y. Zhang, X. Zhang, H. Zhang, Enhancement of properties of rapeseed straw/polyvinyl chloride composites by ultrasonically driven attapulgite loading and its mechanism, Construct. Build Mater. 496 (2025) 143799, https://doi.org/10.1016/J.CONBUILDMAT.2025.143799.
[17] M. Wang, Q. Jun, H. Xie, X. Tao, L. Tan, C. Wu, Uptake properties of Eu(III) on Na-attapulgite as a function of pH, ionic strength and temperature, J. Radioanal. Nucl. Chem. 292 (2011) 763–770, https://doi.org/10.1007/S10967-011-1517-9.
[18] Q. Fan, D. Shao, Y. Lu, W. Wu, X. Wang, Effect of pH, ionic strength, temperature and humic substances on the sorption of Ni(II) to Na–attapulgite, Chem. Eng. J. 150 (2009) 188–195, https://doi.org/10.1016/J.CEJ.2008.12.024.
[19] C. Fu, X. Zhu, X. Dong, P. Zhao, Z. Wang, Study of adsorption property and mechanism of lead(II) and cadmium(II) onto sulfhydryl modified attapulgite, Arab. J. Chem. 14 (2021) 102960, https://doi.org/10.1016/J.ARABJC.2020.102960.
[20] Q. Yang, H. Wang, Y. Zhong, G. Lu, Z. Dang, L. Zhang, Co-adsorption behaviors and mechanisms of cd(II), pb(II), and Cr(VI) on sodium dodecyl sulfate modified attapulgite clay-supported nano zero-valent iron: competitive or synergistic effect? Environ. Res. 271 (2025) 121107 https://doi.org/10.1016/J.ENVRES.2025.121107.
[21] G. Zhang, Z. He, W. Xu, A low-cost and high efficient zirconium-modified-Na-attapulgite adsorbent for fluoride removal from aqueous solutions, Chem. Eng. J. 183 (2012) 315–324, https://doi.org/10.1016/J.CEJ.2011.12.085.
[22] D. Chen, Y. Du, H. Zhu, Y. Deng, Synthesis and characterization of a microfibrous TiO_2–CdS/palygorskite nanostructured material with enhanced visible-light photocatalytic activity, Appl. Clay Sci. 87 (2014) 285–291, https://doi.org/10.1016/J.CLAY.2013.11.031.
[23] H. Sun, J. Wang, Y. Zong, J. An, Y. Jing, F. Wang, J. Li, A. Li, Hofmeister effect-inspired attapulgite-based monoliths for stable solar-driven interfacial vapor generation with salt and acid resistance, Desalination 602 (2025) 118651, https://doi.org/10.1016/J.DESAL.2025.118651.
[24] G. Hekimoğlu, A. Sarı, Shape stabilized attapulgite/myristic-palmitic acid composite PCM for thermal energy storage implementations in buildings, Mater. Today Proc. 58 (2022) 1350–1353, https://doi.org/10.1016/J.MATPR.2022.02.229.
[25] W. Zhan, Y. Zhao, Y. Yuan, H. Yi, S. Song, Development of 2D-Mt/SA/AgNPs microencapsulation phase change materials for solar energy storage with enhancement of thermal conductivity and latent heat capacity, Sol. Energy Mater. Sol. Cells 201 (2019) 110090, https://doi.org/10.1016/j.solmat.2019.110090.
[26] N. Wang, J. Liu, C. Li, X. Wang, Q. Zhang, F. Yuan, Z. Sun, Molten salt activation induced porous graphitic carbon/attapulgite composites as superior adsorbent for multiple mycotoxins, Miner. Eng. 234 (2025) 109719, https://doi.org/10.1016/J.MINENG.2025.109719.
[27] Y. Wang, S. Jia, S. Ding, W. Zhang, R. Shu, Y. Hu, Development of Palygorskite-$CaIn_2S_4$ composite for rapid Cr(VI) reduction under visible light, J. Environ. Sci. 156 (2025) 562–575, https://doi.org/10.1016/J.JES.2025.02.021.
[28] W. Zhan, F. Jia, Y. Yuan, C. Liu, K. Sun, B. Yang, S. Song, Controllable incorporation of oxygen in MoS_2 for efficient adsorption of Hg^{2+} in aqueous solutions, J. Hazard. Mater. 384 (2020) 121382, https://doi.org/10.1016/j.jhazmat.2019.121382.
[29] K. Li, C. Li, N. Wang, R. Ma, S. Li, Effective enrichment of Cs^+ and Rb^+ from high-salty solutions using calcium hexacyanoferrate and followed separation by phase-transformation, Desalination 603 (2025) 118667, https://doi.org/10.1016/J.DESAL.2025.118667.